Warpage deformation analysis of AMB ceramic substrates in power modules

Hu, Dong; Wang, Chieh; Li, Zichuan; Gupta, Nikhil; Poelma, René H.; Shi, Ziliang ; Fan, Jiajie; Zhang, Guoqi

DOI
10.1109/EuroSimE60745.2024.10491425

Publication date
2024

Document Version
Final published version

Published in
Proceedings of the 2024 25th International Conference on Thermal, Mechanical and Multi-Physics Simulation and Experiments in Microelectronics and Microsystems (EuroSimE)

Citation (APA)
Hu, D., Wang, C., Li, Z., Gupta, N., Poelma, R. H., Shi, Z., Fan, J., & Zhang, G. (2024). Warpage deformation analysis of AMB ceramic substrates in power modules. In *Proceedings of the 2024 25th International Conference on Thermal, Mechanical and Multi-Physics Simulation and Experiments in Microelectronics and Microsystems (EuroSimE)* (2024 25th International Conference on Thermal, Mechanical and Multi-Physics Simulation and Experiments in Microelectronics and Microsystems, EuroSimE 2024). IEEE. https://doi.org/10.1109/EuroSimE60745.2024.10491425

2024 25th International Conference on Thermal, Mechanical and Multi-Physics Simulation and Experiments in Microelectronics and Microsystems (EuroSimE) | 979-8-3503-9363-7/24/$31.00 ©2024 IEEE | DOI: 10.1109/EuroSimE60745.2024.10491425

Warpage deformation analysis of AMB ceramic substrates in power modules

Dong Hu[1], Chieh Wang[1], Zichuan Li[1], Nikhil Gupta[1], René H. Poelma[1,2], Ziliang Shi[2], Jiajie Fan[1,3,4], Guoqi Zhang[1*]
1 EEMCS Faculty, Delft University of Technology, Delft, the Netherlands
2 Nexperia B.V., Nijmegen, the Netherlands
3 Institute of Future Lighting, Academy for Engineering & Technology; Shanghai Engineering Technology Research Center for SiC Power Device, Fudan University, Shanghai 200433, China
4 Research Institute of Fudan University in Ningbo, Ningbo 315336, China
*Corresponding author: Guoqi Zhang, Email: G.Q. Zhang@tudelft.nl

Abstract

Driven by the increasing demand for high-power systems, ceramic substrates have received more attention for handling higher power density. Warpage in active metal brazed (AMB) ceramic substrate becomes a critical issue as it can deteriorate the reliability performance. This study comprises three phases, including investigation of the cause of the warpage, validation of the proposed model, and optimization for effective warpage management. At first, the coefficient of thermal expansion (CTE) and yield strength of the copper (Cu) layer in AMB were characterized and adopted in a two-dimensional (2D) finite element model. The evolution of simulated strain and moments revealed the cause of the warpage during the manufacturing processes. Furthermore, the 2D model was extended to a three-dimensional (3D) model. The finite element method (FEM) and experiments were conducted on different heat treatment conditions for 3D model validation. The validated 3D model was applied to carry out a design of experiments (DoEs) for design optimization to reduce the warpage. Consequently, the factor analysis in DoEs was demonstrated by different pattern designs using subtractive milling techniques.

1. Introduction

Electrical vehicles (EVs) and hybrid-electric vehicles (HEVs) are penetrating the transportation market. Thus, the increasing demand for higher power (> 200 kW) and higher voltage rating (> 800 V) drives the rapid development of power electronics as one critical strategic direction in the 'More than Moore' paradigm toward high performance and efficiency [1]–[3]. In particular, wide-bandgap (WBG) semiconductors, represented by silicon carbide (SiC) and gallium nitride (GaN), have been proposed to boost the performance of EVs and HEVs to overcome the physical limit of silicon-based devices [4], [5].

Power electronics can be integrated discretely within one power module package. Printed circuit boards (PCBs) are not applicable in this scenario due to high working current and voltage. To connect electronics components within the power module, ceramic substrates, such as aluminum oxide (Al_2O_3, CTE: 4.5×10^{-6} °C^{-1}) [6], aluminum nitride (AlN, CTE: 4.3×10^{-6} °C^{-1}) [7], and silicon nitride (Si_3N_4, CTE: 2.6×10^{-6} °C^{-1}) [8], [9], are widely used because of excellent insulation capability and thermal conductivity.

In general, the ceramic substrates can be divided by the metallization approaches, such as direct bonded copper (DBC) and AMB [10], [11]. Unlike DBC, which utilizes the eutectic melting temperature (>1065 °C) of the metal and the ceramic, the AMB technique uses an active metal layer containing silver (Ag), titanium (Ti), and Cu to form a metallurgical combination layer at a brazing temperature of 800 °C. The active metal layer of the AMB substrates generates a more potent bonding force and less thermal stress, resulting in higher reliability than the DBC substrates [12], [13].

Despite the reduced thermal stress in the AMB substrates, the significant CTE differences between the Cu (16.7×10^{-6}/°C) and ceramic layer can cause massive warpage with residual stress from the heat treatment in its manufacturing and further back-end processing [14]. Warpage is a critical issue as it can introduce micro-cracks in the brittle ceramic layer and also the delamination of the active metal solder interface [15]. The reduced mechanical performance and thermal management significantly deteriorate the system performance. Hence, the causes of warpage resulting from the manufacturing need to be clarified. Additionally, an effective warpage management methodology is required in the design guidelines.

In this study, the thermo-mechanical response of brazed Cu was characterized by a thermomechanical analyzer (TMA) and high-temperature tensile tests. The extracted parameters were subsequently adopted to improve a FEM model on a Si_3N_4 AMB substrate. The FEM model was first validated according to the post-anneal warpage and then extended to investigate the geometric influence factors in an AMB, which was consequently verified by mechanical milling-modified AMB components. This work explains the causes of warpages in as-manufactured AMB components and also paves the way for effective warpage management from a design view.

2. Methods

2.1. Thermo-mechanical Characterization

An accurate material model is essential to finite element analysis (FEA). An oxygen-free copper (OFC) sheet from an AMB manufacturer experienced the identical heat treatment process as AMB substrates. The OFC sheet was 800 μm, the same Cu layer thickness in AMB substrates. The properties of OFC Cu in the AMB substrate differ from the original status because of long-time high-temperature annealing. The coarse grains were visible in the annealed OFC compared to the unannealed samples, as shown in Fig. 1.

979-8-3503-9363-7/24/$31.00 ©2024 IEEE

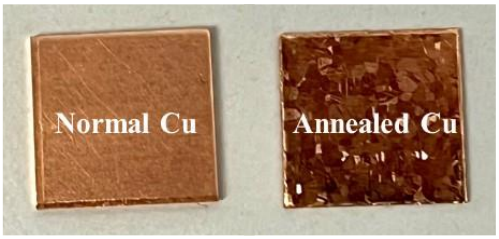

Figure 1. The unannealed OFC (left) and annealed OFC (right) were studied in this study. Grain boundaries can be recognized with eyes.

The annealed OFC sheet was first cut into 8 mm × 4 mm for identifying CTE values. A Mettler Toledo TMA SDTA2+ equipment was employed to measure the thermal expansion up to 365 °C with a ramping rate of 5 °C/min. The linear CTE (α) can be expressed using the equation:

$$\alpha = \frac{1}{L_0} * \frac{d(\Delta L_T)}{dT} \quad (1)$$

where L_0 is the sample length, and L_T is the length change at temperature T.

Subsequently, constant strain-rate high-temperature tensile tests were conducted ranging from 20 °C to 250 °C. The strain rate was fixed as 0.1 s^{-1}. As shown in Fig. 2, the dog-bone-shaped specimen was prepared with an effective dimension of 5 mm × 25 mm × 0.8 mm. A MTS CMT 4303 tensile tester was employed in this study. Fig.2 depicts the crosshead arrangement used to hold the tensile sample in place during the test. The applied force and the displacement of the crosshead were recorded until the sample fracture.

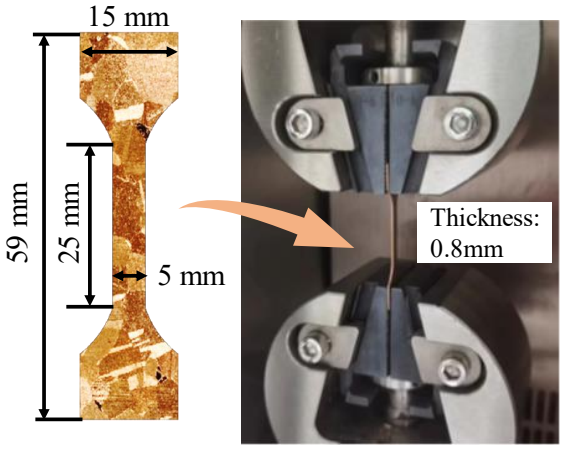

Figure 2. Schematic of dog-bone-shaped sample and its mounting on the tensile equipment.

2.2. Warpage measurement

This study used a non-contact Keyence VK-X250 3D laser scanning microscope equipped with a 10× magnification lens to capture the top surface of the AMB substrates. The warpage value was defined by subtracting the highest point minus the lowest point on the same profile, the midline on the top surface with the sample stage as zero reference plane.

2.3. Subtractive manufacturing process

Different patterns in the Cu layer in AMB substrates were implemented by mechanical milling. A mechanical milling tool that used a rotary cutter at a spinning speed of 12732 rpm and feeds 255 mm/min was employed to remove excessive Cu materials.

2.4. Heat treatment process

Heat treatment to the analog sintering process was conducted in a die-bonder chamber (Tresky T3000-Pro) with an inert N_2 atmosphere. The analog sintering profile is 280 °C for 10 minutes with a fast ramping rate of 20 °C/min. After heat treatment, the AMB substrates were rapidly cooled down with compressed air.

2.5. Finite Element Simulation

A thermo-mechanical FEM simulation is used to describe the warpage of the AMB substrates under different conditions. COMSOL Multiphysics 6.1 was used in this study with thermo-mechanical coupled modules.

Figure 3 presents the mesh and boundary settings used to simulate 2D deformation. The model comprised three layers, from top to bottom: a 0.8mm Cu layer, a 0.32 mm Si_3N_4 layer, and again a 0.8mm Cu layer at the bottom. The geometry was meshed with free tetrahedral shapes. Considering the thin structure, the maximum element size is 0.1 mm, and the minimum element size is 0.001 mm. The two-point boundary condition was set as the left bottom corner point had a prescribed zero displacement in both the *x* and *y* directions. In contrast, the right bottom corner point had only a prescribed zero displacement in the y displacement. This setting prevented the rotation and slip on the surface and captured the deformation accurately during the FEM simulations.

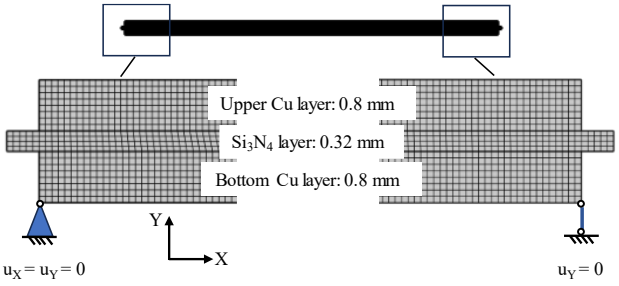

Figure 3. Meshing and boundary conditions of a 2D FEM model. The layers from top to bottom are the upper Cu layer, the middle ceramic layer, and the bottom Cu layer.

3. Results and discussion

3.1. OFC characterization

The evolution of sample thickness in the cooling phase from 365 °C to 25 °C was present in Fig. 4. A linear fitting was estimated, and the fitted slope was calculated as 0.0137 μm/°C. The thickness at 25 °C can be estimated as the original thickness of 813.6 μm. Hence, Eq. 1 calculated the CTE value of annealed OFC as 16.8 ppm/°C. This value

doesn't differ from normal Cu at 16.7 ppm/°C. This is because the crystal constant dominates the CTE rather than other crystallographic information, such as grain size, grain boundary, and orientation.

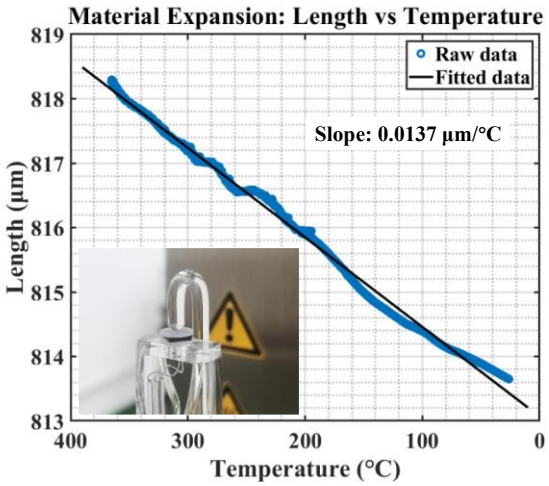

Figure 4. Evolution of annealed OFC expansion in the cooling phase from 365 °C to 25 °C. The inserted frame shows how the thickness is measured.

Figure 5(a) illustrates the stress-strain curve of annealed OFC at 20 °C, 95 °C, 170 °C and 250 °C. It can be seen that the sample quickly yielded at a low strength, which was caused by the coarse grain structure. Afterward, the stress gradually increases with a slightly increased tangent modulus. When the temperature increases, a higher plasticity and lower tensile strength are figured out.

Figure 5(b) shows the initial deformation stage of all samples. The elastic modulus was, therefore, extracted by the slope of the first linear part of the stress-strain curve. Yield stress was calculated as the stress value corresponding to 0.2% strain offset. In addition, the evolution of tangent modulus in the plastic regime was not significant. Therefore, the tangent modulus was estimated as the slope for the segment between the yield point and the ultimate tensile stress point.

The material properties are summarized in Table 1. The measured yield stress and tangent modulus present a declining trend against the temperature increase.

However, the elastic modulus was much lower than other annealed Cu reported in [16]. In the opposite direction of the size effect, the elastic modulus stays relatively stable when the grain size is larger than 50 nm [17]. This study estimated a grain size of roughly 733.4 µm by calculating the number of grains over random lines in the surface morphology. Hence, the elastic modulus obtained from this tensile test cannot be enriched to FEM simulation. The underestimation of the elastic modulus can be attributed to the strain calculation methods. In this case, the strain was not directly measured by the strain gauge in the effective region but calculated by the displacement traveled by the upper clamping component. Therefore, the obtained displacement also contained other displacement, such as the slippage of the gripper, clamping deficiencies, and the movement of the crosshead. This overestimation of the displacement results in a misguided larger plasticity and, therefore, smaller elastic modulus.

Regarding the rest of the measured properties, the yield stress was referred to as the stress at a 0.2% offset already in the plastic regime. As the plastic deformation behavior remains the same, in case of underestimating the elasticity, the yield points would shift leftward, but the yield stress would remain the same. In [18], it has also been demonstrated that the yield stress is mostly independent of equipment variables, gripping effects, and measurement errors.

The same conclusion also goes to the obtained tangent modulus. The overestimated displacement was significant in the elastic region. However, the overestimated value became negligible compared to the measured fracture strain (> 20%). Hence, the measured tangent modulus would also apply to the FEM model in the following section.

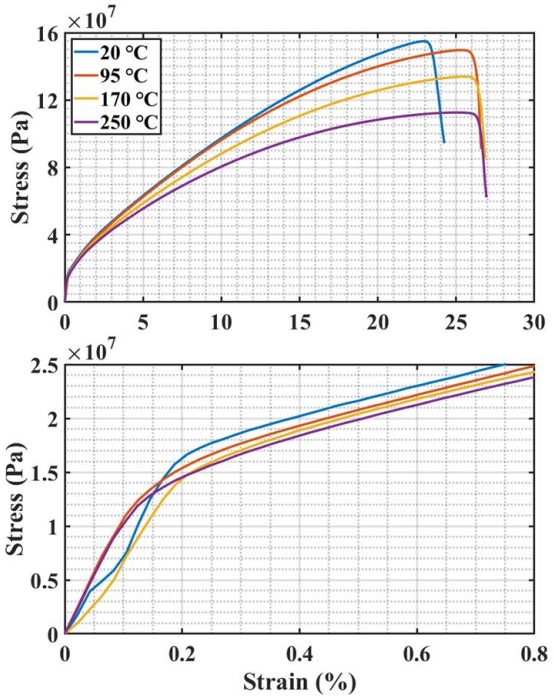

Figure 5. (a) Stress-strain curves of the annealed OFC samples. (b) Zoom in with the first 0.8% strain.

Table 1. Summary of tensile results of annealed OFC samples.

Temperature [°C]	Elastic modulus [GPa]	Yield stress [MPa]	Tangent modulus [MPa]
20	10.5	18.8	674.4
95	10.2	17.5	684.6
170	9.1	17.3	591.7
250	10.4	16.3	507.7

3.2. Warpage analysis in 2D FEM model

The as-received AMB substrate (53 mm × 39 mm) already held an initial warpage of 66.72 µm. This value

incredibly increased to 286.25 μm after a 10-min 280 °C annealing process in the N_2 environment.

Two significant heat treatment processes affect the warpage in the AMB substrates. The first is in the brazing process, where the brazed components cool down from 800 °C to 20 °C. This significant temperature reduction incorporated Cu volume shrinkage on both sides. After the topside patterning process by chemical etching at room temperature, the unbalanced stress caused the initial warpage. Moreover, since the stress-free temperature is the brazing temperature, 800 °C, the annealing process further warped the AMB substrate. A 2D FEM model in this study revealed the initial warpage and the further warpage.

Table 2 lists the material properties. CTE, yield stress, and tangent modulus of Cu were derived from this study, and the other parameters were referred to other research. The temperature dependency of Si3N4 was skipped for simplification. A linear estimation with temperature was made for elastic modulus, yield stress, and tangent modulus of Cu. Only isotropic tangent modulus was input for a perfect plasticity assumption because this simulation work does not consider fracture and delamination phenomena.

Table 2. Material properties of Si_3N_4 and Cu in the FEM model. T is the value of temperature in unit °C.

Materials	Si_3N_4 [14]	Cu [16]
Elastic modulus [GPa]	300	-0.0513T+95.2
Poisson's ratio	0.28	0.34
CTE [$\times 10^{-6}$ °C^{-1}]	2.6	16.8 (This work)
Yield Stress [MPa]	/	-0.0101T +18.8214 (This work)
Tangent modulus [MPa]	/	-0.778T +718.6617 (This work)

During the simulation process, five steps were taken in the stationary study. These steps are analogous to the manufacturing and annealing process, as shown in Figure 6. The measured actual warpage was also given. Steps 1-3 are the AMB manufacturing processes. In Step 1, the entire model was conducted at 800 °C. Next, the simulation environment temperature was cooled to 20 °C. Step 3 removed some patterns on the upper Cu layer using the deactivation function, where the elastic stiffness and density of the selected domain were reduced to 10^{-5} times their original values. Step 4 & 5 is the annealing die-attach process. The patterned model was re-conducted to 280 °C. Lastly, Step 5 cooled the unsymmetrical model back to 20 °C. In these two steps, the AMB substrate experienced a transition from convex warpage to concave warpage and back to convex warpage at the end.

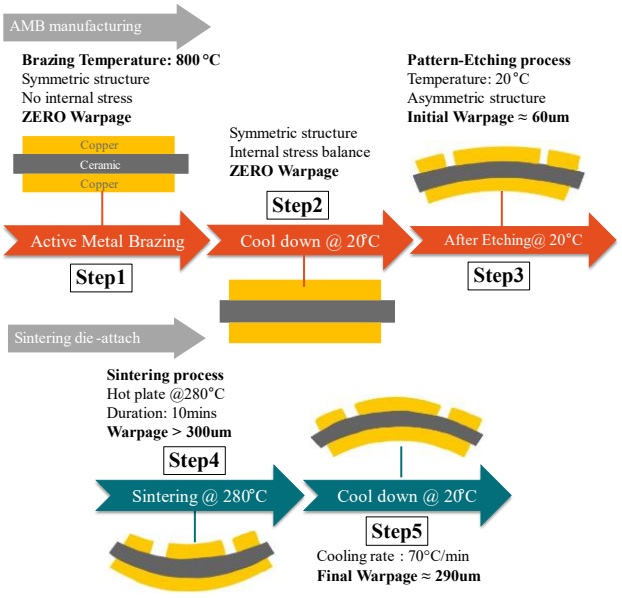

Figure 6. Schematic of warpage evolution in AMB substrate regarding different manufacturing processes.

The warpage analysis was separated into two parts, as stress can be translated into strain in *XX* direction in horizontal direction and moment in vertical deformation.

The composition of total strain ε in Cu can be expressed as

$$\varepsilon = \varepsilon_t + \varepsilon_e + \varepsilon_p \quad (2)$$

$$\varepsilon_t = \alpha(T - T_{ref}) \quad (3)$$

where ε_t, ε_e, and ε_p are the thermal, elastic, and plastic strain along the *XX* direction, respectively. The thermal strain refers to the thermal expansion or contraction. α is the CTE of Cu, T is the temperature, and T_{ref} is the reference temperature of 800 °C. The elastic strain refers to the reversible strain caused by the force. The plastic strain, on the other hand, refers to the irreversible strain when the force exceeds the yield stress of Cu.

Figure 7 depicts the evolution of the aforementioned strain from Step 2 to Step 5. It can be seen that due to low yield stress, the deformation is primarily dominated by thermal strain and plastic strain.

In the cooling phase in Step 2, the Cu layer undergoes more shrinkage than the ceramic layer because of much higher CTE. However, the brazed parts were strongly connected, and there was no relative displacement between the Cu and ceramic layers. Therefore, the Cu layers were subjected to tensile forces, while the ceramic layer was subjected to compressive forces to balance thermal contraction. The simulated Von Mises stress in both Cu layers is around 26.2 MPa, indicating nearly 1.1% plastic strain in the Cu layers. However, due to the same Cu volume in the upper and bottom layers, a symmetric structure was kept with zero warpage despite significant inner stress.

Step 3 transfers the pattern to the upper Cu layer using a chemical etching process at room temperature. Therefore, there was no change in the thermal strain. However,

removing Cu reduced stress levels around the trench areas, further disrupting the balance of inner tensile stress. The stress release, on the one hand, slightly decreased the average strain distribution. On the other hand, a convex shape was first formed in the AMB substrate, as shown in Fig. 7.

Subsequently, the temperature increase in Step 4 reduced the thermal strain because the difference between actual and reference temperatures is much smaller. However, the volume of Cu in the upper layer and bottom layer is unbalanced. More Cu in the bottom generated a more significant expansion force, causing a transformation in shape from convex to concave.

At last, in Step 5, the AMB substrate was simulated back to 20 °C, indicating the same thermal strain as in Steps 2 & 3. However, the non-reversible plastic deformation had already compressed slightly back in Step 4 when the warpage direction changed. The average plastic strain after Step 5 is 1.06%. Although more prominent than the value of 0.8% in Step 4, this value failed to reach the level in Step 3 of 1.09%. In terms of the elastic deformation, the elastic strain experienced a slight increase from 0.02% to 0.03% from Step 3 to Step 5. However, the decrease in the plastic strain was more significant than the increase in the elastic strain. As shown in Fig. 7, the negative plastic strain indicated the outward plastic deformation. Hence, a more severe convex warpage after Step 5 can be explained from the strain perspective in the *XX* direction.

In addition to the strain distribution over the steps, the influence of different steps on the moment was also investigated. The moment τ can be expressed as

$$\tau = r \times F = \frac{d^2 v}{dx^2} EI \qquad (4)$$

where r is a vector from the force of the moment measure point. F is force, the second derivative d^2v/dx^2 is the curvature in the slight deflection. The ceramic's upper edge profile was applied to calculate this term. EI is flexural rigidity.

Figure 7(b) illustrates the evolution of the moment over Step 2 to Step 5, plotted with the total strain at each step. The same evolution trend is figured out in both moment and total strain, corresponding to the variation in actual warpage deformation.

The moment was first kept at zero until the etching process in Step 3, where it became a negative value. In the next step, the moment changed to a positive value at 280 °C, indicating the warping direction changed from convex to concave. Finally, during the cooling session in Step 5, the moment decreased further to a more considerable negative value than in Step 3. This trend in moment values reflects the corresponding changes in warpage deformation.

Compared with the strain value change, although a similar trend, the moment can better reflect the generation of the initial warpage as more vertical displacement occurred. Thus, the moment is a crucial factor influencing the warpage deformation during the processes.

In summary, the observed warpage change was successfully mirrored by the proposed 2D model. The warpage was revealed to be primarily induced by variation in moments within the substrate. The first warpage arose from the elastic strain imbalance after the etching process. In contrast, a more severe final convex warpage was attributed to more outward plastic deformation.

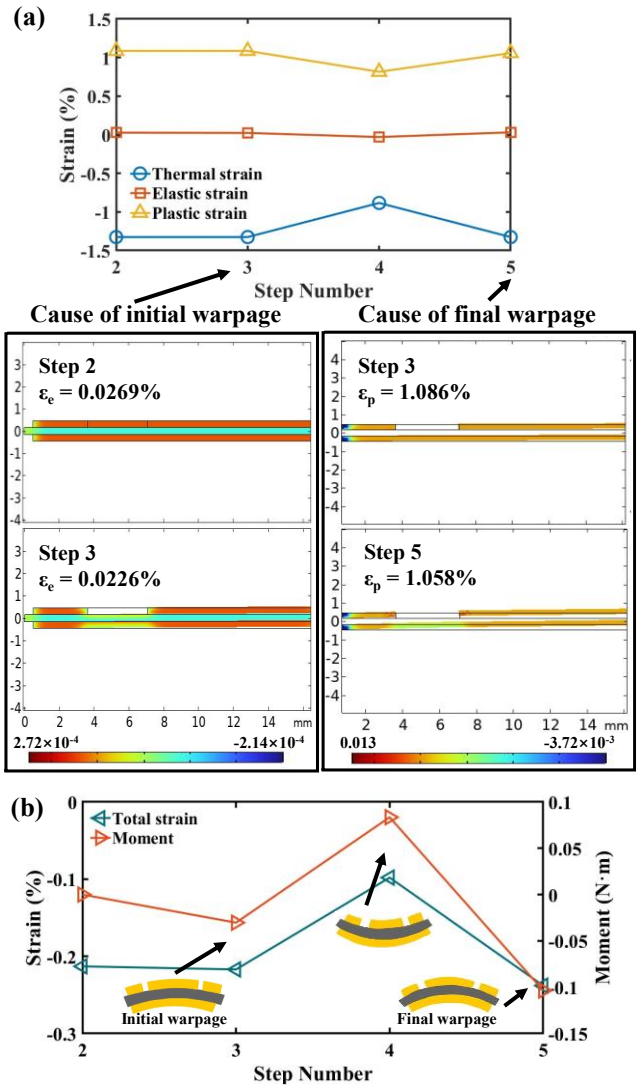

Figure 7. (a) Average strain in Cu layers from Step 2 to Step 5. The strain change that caused the initial and final warpage was displayed in the frames. (b) Evolution of moment and total strain from Step 2 to Step 5.

3.3. Warpage analysis in heat treatment

To further validate the FEM model, a 3D model based on the actual geometry was constructed. The final warpage was measured and simulated at various annealing temperatures ranging from 140 °C to 280 °C. The comparison between simulation and experiments is presented in Fig. 8(a). The warpage change is the ratio of the final warpage to the initial warpage. Both simulation and experimental results show an increasing trend in the final warpage according to the annealing temperature increase. However, it is observed that experimental results

exhibit a more significant change in warpage compared to simulation results. This deviation can be caused by inaccuracy in the material model. First, the thermo-mechanical tests were carried out until 250 °C and a simple linear dependency was estimated. Therefore, the description of temperature-dependent properties can be inaccurate over 250 °C. It can be seen that the difference between simulated warpage change and measured warpage change becomes larger after 230 °C. As explained, the measured tangent modulus can differ slightly due to the wrong strain estimation. Besides, the elastic modulus was referred from other AMB-related work. Hence, the value can be different due to different AMB manufacturers.

In addition to different annealing temperatures, the reproductivity was also simulated. The AMB substrates underwent an annealing process at 280 °C three times. The measured results, together with the corresponding FEM simulation results, are plotted in Fig. 8. In both simulation and experiment results, the warpage became more severe with more thermal cycles. However, it was noticed that the most substantial warpage change occurred after the first annealing session. In contrast, the warpage increase in the subsequent second and third annealing sessions was not remarkable. The increased warpage can be attributed to the accumulated plastic deformation. Besides, there was no substantial difference in the warpage between the FEM simulation and the measured results.

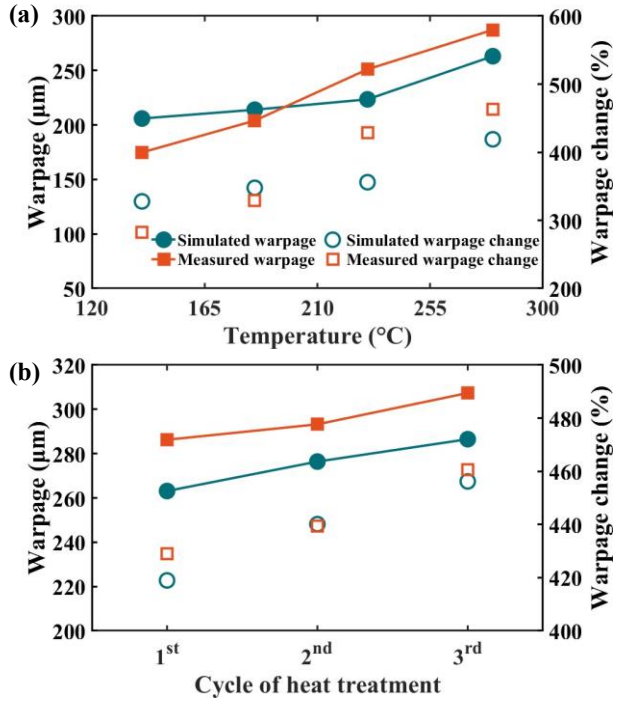

Figure 8. The simulated and measured warpage with (a) different annealing temperatures and (b) different cycles of 280 °C annealing sessions. The initial warpage of simulation and measurement is 62.8 μm and 66.7 μm, respectively.

As a result, despite the slight difference in the absolute numbers, a compelling alignment between the simulation and experiment results is evident. This congruence underscores the simulation's capacity to replicate the experimental outcome, thereby confirming the validation of the FEM model through experimental verification. This robustly validated model will be applied in the next section to find a solution for effective warpage management.

3.4. Factor analysis on effective warpage management

The aforementioned validated FEM model can investigate the impact of Cu's pattern design factor on warpage. A simplified structure was created, as shown in Fig. 9. The structure comprises three Cu pads of identical length and width on the upper layer, as well as a complete Cu pad in the bottom layer, which mimics the actual AMB substrate that an upper Cu layer contains several islands with different functionalities.

In the DoEs, six variables were considered to investigate the influence of the Cu thickness, edge gap, and trench width on the final warpage performance. As indicated in Fig.9, Cu_s, Cu_m, and Cu_b represent the thickness of two-sided Cu pads on the top side, the middle Cu pad on the top side, and the Cu pad on the bottom side, respectively. Considering the actual thickness of the AMB, values between 0.3 to 0.8 mm were chosen. Regarding the edge between Cu pads and the ceramic edge in both x and y directions, gap_f and gap_b signify the value on the topside and bottom side, respectively. The spacing between Cu pads on the topside was defined as gap. The values of gap_f, gap_b, and gap were set explicitly from 0.5 mm to 1.5 mm.

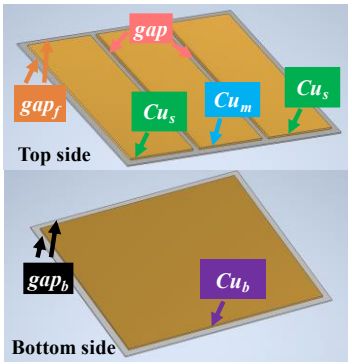

Table of the symbol and value range of the influence factors

Variables		Min.	Max.
Thickness [mm]	Cu_s	0.3	0.8
	Cu_m	0.3	0.8
	Cu_b	0.3	0.8
Edge [mm]	gap_f	0.5	1.5
	gap_b	0.5	1.5
Trench [mm]	gap	0.5	1.5

Figure 9. Schematic of the AMB model for influence factor analysis. The value range of the influence factors is included.

Subsequently, all combinations outlined in Fig. 9 were simulated by a parametric sweep function. Response surface methodology (RSM) was utilized to investigate the significance of different variables. In this study, Design Expert software and the analysis of variance (ANOVA) method were employed, with which the parameter that has the most significant impact on the dependent variable was identified, and the relationship between the dependent and independent variables was established.

In this study, a linear model (Eq. 5) was chosen to assess the p-value to determine the significance and adaptability of the coefficient of determination.

$$DV = \beta_0 + \sum_{i=1}^{k} \beta_i x_i \quad (5)$$

where DV is the dependent variable, β_0 and β_i are regression coefficients for intercept and linear coefficients, respectively, and x_i is the independent variable.

Table 3 shows the results of the statistical analysis of model fitting. The proposed linear model was valid with a *P*-value smaller than 0.001. Besides, the measurement of R^2 was 0.98, indicating a great fitting in the proposed model. In terms of the independent variables, the thickness of Cu pads showed great significance with a *P*-value smaller than 0.001. The thickness of the Cu pad on the bottom side was revealed as the most significant variable according to the largest *F*-value of 3099.2. In contrast, gap_f and gap_b are relatively insignificant compared to the thickness of the Cu pad. The spacing between the Cu pads *gap* shows limited significance to the final warpage results.

Table 3. The warpage model fitting results correspond to different independent variables.

Source	Sum of squares	*F*-value	*P*-value
Model	4.4×10^7	686.7	<0.001
Cu_s	6.1×10^7	563.7	<0.001
Cu_m	7.9×10^7	735.8	<0.001
Cu_b	3.4×10^7	3099.2	<0.001
gap_f	7.4×10^3	0.7	0.41
gap_b	6.7×10^3	0.6	0.43
gap	4.9×10^4	46	0.0358

As a result of the DOEs study, a parameterized equation of Eq. 5 can be given as expressed in Eq. 6.

$$\begin{aligned} Warpage &= 91.23 \\ &-284.6Cu_s - 324.13Cu_m + 613.56Cu_b \\ &+10.34gap_f - 9.82gap_b + 25.76gap \end{aligned} \quad (6)$$

The coefficient value quantitatively represents the significance of the independent variables on the warpage performance. It can be seen that the thickness of the Cu pads primarily dominated the warpage. Accounting into the symbols of Cu_s, Cu_m, and Cu_b, a balance of the copper volume on the topside and bottom side is essential to reduce the warpage. A slight reduction in Cub can be amplified into a significant improvement in warpage. In the optimal design, the bottom side Cu thickness Cu_b was reduced from 0.8 mm to 0.74 mm, and the trench width *gap* increased from 0.5 mm to 1.5 mm. The warpage with optimal parameters was 26.1 μm, approximately 25% of the original warpage of 103.6 μm.

As demonstrated in the simulation, the warpage is significantly influenced by the unbalanced Cu volume in the upper and bottom layers. Patterning the bottom Cu layer could be a solution to reduce the warpage because the pattern on the top side can result from other multi-physics optimization concerns more than the warpage, for example, the parasitic inductance and thermal management. Therefore, mechanical milling-enabled subtractive manufacturing on the bottom Cu layer was carried out to verify the hypothesis.

The pattern design initiative began with a basic rectangular ring structure, chosen to simplify and facilitate dimensional analysis by adjusting the width and length parameters while also considering processing convenience. Four distinct pattern designs were implemented on the bottom Cu layer in AMB substrates with original dimensions of 44.4 mm × 49 mm, named *S0*, *S1*, *S2,* and *S3*, as shown in Fig. 10(a)-(d). Design *S1* features a small rectangular ring with a trench width of 1.5 mm and a depth of 0.4 mm. The outline and depth of the trenches are fixed in *S2* and *S3* as 34.4 mm × 35 mm and 0.4 mm. In comparison, *S2* has a medium rectangular ring with a width of 3 mm. The widths in the *S3* are 4.4 mm and 5 mm, respectively. *S0* is untreated as the reference.

The removed Cu volume is 79.64 mm^3, 152.16 mm^3, 225.6 mm^3 in *S1* to *S3*, respectively. The initial warpage before the subtractive manufacturing was 44.1 μm, 49.97 μm, 49.15 μm, 50.28 μm for non-milled AMB and design *S1* to *S3*. Subsequently, all designs were subjected to a 280 °C annealing process, and the final warpage was measured afterward. The warpage change was calculated to avoid the difference from the initial warpage value.

The relationship between the final warpage change and milled Cu volume is plotted in Fig. 10(e). An evident decrease trend was observed with more Cu volume milled out. The reduction of warpage is relatively linear to the milled Cu volume. In the non-patterned *S0*, the warpage change reached 324.7%, while this value significantly dropped to 102% in the case of design *S3*. Incredible warpage reduction in design *S1* and *S2* was also observed, at 234% and 193%, respectively.

Therefore, the warpage reduction can be translated to a balance issue between the upper Cu layer and the bottom Cu layer. In the current product, where Cu layers in the upper layer and bottom layer share the same thickness, the reduction of the bottom Cu layer has been demonstrated as the most effective method to manage the warpage from both perspectives of FEM simulation and experiments.

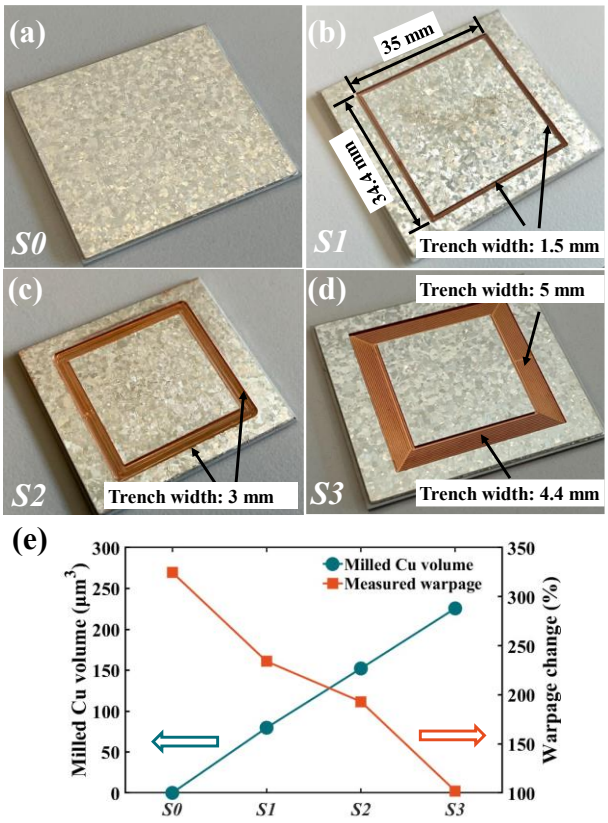

Figure 10. (a)-(d) Original and subtractive manufactured AMB substrates with different pattern designs (S0 – S3) on the bottom Cu layer. (e) The relationship between final warpage change and milled Cu volume.

4. Conclusions

Driven by the rapid development of power electronics, the reliability of power modules has become a primary concern to ensure performance. Warpage, caused by thermo-mechanical stress at the interface, poses a risk of cracks and delamination in the system. This study first investigated the basic material properties of the AMB substrate and further integrated them into FEM simulations. A 2D model revealed the underlying reason for warpage. Afterward, a validated 3D FEM simulation-based optimization was carried out and consequently verified by experiments. This work paves the way for more effective warpage management in the AMB substrate, which could be crucial in the future power module design. The following conclusions were obtained:

1) A 2D FEM model with materials properties extracted from experiments was built up. The CTE of annealed OFC was measured as 16.7 ppm/°C, and the yield strength was measured as 18.8 MPa, 17.51 MPa, 17.3 MPa, and 16.3 MPa at 20 °C, 95 °C, 170 °C and 250 °C, respectively. The model's accuracy was confirmed by its alignment with experimental trends, reaffirming its validity.

2) The validated 2D FEM model revealed the mechanical behavior during the manufacturing process. The evolution of thermo/elastic/plastic strains and moments were simulated at each manufacturing step. Due to the different patterns on the upper and bottom Cu layer, the generation of the final warpage was revealed as the plastic strain difference, which showed 3.5 times the elastic strain difference.

3) A 3D FEM model extended from a 2D model was built up. Warpage behavior with different heat treatments, i.e., different annealing temperatures and different annealing cycles, were measured and simulated, respectively. A higher annealing temperature would significantly increase the warpage. More annealing cycles also contributed slightly to a more considerable warpage. The comparison of simulation and experimental findings proved a high correspondence in the proposed 3D FEM model.

4) In a 3D FEM model, DoEs covering the thickness of the Cu layer and the spacing between Cu pads and edge gaps were conducted by RSM analysis, where a linear model was parameterized. The primary factor to mitigate warpage was the balance of the Cu volume. The simulated optimal design presented a 74.8% warpage reduction by reducing the thickness of the bottom Cu layer. Subtractive manufacturing was therefore conducted on the bottom Cu layer with different milled Cu volumes. With more Cu milled out, the warpage change was incredibly reduced from 324.7% to 102%. Hence, the manipulation of Cu volume validated the warpage alleviation.

Acknowledgments

This work was supported by the National Natural Science Foundation of China (Grant No. 52275559).

References

1. S. Thangavel, D. Mohanraj, T. Girijaprasanna, S. Raju, C. Dhanamjayulu, and S. M. Muyeen, "A Comprehensive Review on Electric Vehicle: Battery Management System, Charging Station, Traction Motors," *IEEE Access*, vol. 11, no. March, pp. 20994–21019, 2023.
2. S. S. G. Acharige, M. E. Haque, M. T. Arif, N. Hosseinzadeh, K. N. Hasan, and A. M. T. Oo, "Review of Electric Vehicle Charging Technologies, Standards, Architectures, and Converter Configurations," *IEEE Access*, vol. 11, no. April, pp. 41218–41255, 2023.
3. G. Q. Zhang, M. Graef, and F. Van Roosmalen, "The rationale and paradigm of 'More than Moore,'" *Proc. - Electron. Components Technol. Conf.*, vol. 2006, pp. 151–157, 2006.
4. A. Matallana *et al.*, "Power module electronics in HEV/EV applications: New trends in wide-bandgap semiconductor technologies and design aspects," *Renew. Sustain. Energy Rev.*, vol. 113, no. June, p. 109264, 2019.
5. J. Broughton, V. Smet, R. R. Tummala, and Y. K. Joshi, "Review of Thermal Packaging Technologies for Automotive Power Electronics for Traction Purposes," *J. Electron. Packag. Trans. ASME*, vol. 140, no. 4, pp. 1–11, 2018.
6. C. Choe, C. Chen, S. Noh, and K. Suganuma,

"Thermal shock performance of DBA/AMB substrates plated by Ni and Ni-P layers for high-temperature applications of power device modules," *Materials (Basel).*, vol. 11, no. 12, 2018.

7. C. Kuring *et al.*, "GaN-Based Multichip Half-Bridge Power Module Integrated on High-Voltage AlN Ceramic Substrate," *IEEE Trans. Power Electron.*, vol. 37, no. 10, pp. 11896–11910, 2022.
8. T. Okuno, S. Arima, K. Tanabe, G. Tanabe, and Y. Uchida, "Si3n4 substrates with anisotropic thermal conductivity suitable for power module applications," in *PCIM Europe Conference Proceedings*, 2021.
9. D. Kim, Y. Yamamoto, S. Nagao, N. Wakasugi, C. Chen, and K. Suganuma, "Measurement of heat dissipation and thermal-stability of power modules on DBC substrates with various ceramics by SiC Micro-heater chip system and ag sinter joining," *Micromachines*, vol. 10, no. 11, pp. 1–11, 2019.
10. K. Hong, T. H. Lee, J. M. Suh, S. H. Yoon, and H. W. Jang, "Perspectives and challenges in multilayer ceramic capacitors for next generation electronics," *Journal of Materials Chemistry C*, vol. 7, no. 32. 2019.
11. R. Khazaka, L. Mendizabal, D. Henry, and R. Hanna, "Survey of high-temperature reliability of power electronics packaging components," *IEEE Trans. Power Electron.*, vol. 30, no. 5, pp. 2456–2464, 2015.
12. J. Lv, Y. Huang, R. Fu, Y. Ji, B. Wu, and X. Liu, "AlN/Cu composite ceramic substrate fabricated using a novel TiN/AgCuTi composite brazing alloy," *J. Eur. Ceram. Soc.*, vol. 40, no. 15, 2020.
13. Y. Zhang, J. Zhang, and J. Chen, "Effect of interfacial microstructure evolution on the peeling strength and fracture of AMB Cu-metalized AlN substrate," *J. Am. Ceram. Soc.*, vol. 105, no. 1, 2022.
14. R. L. Moran *et al.*, "Reduction of IC Package Warpage through Finite Element Analysis and Direct Optimization," in *2019 IEEE 11th International Conference on Humanoid, Nanotechnology, Information Technology, Communication and Control, Environment, and Management, HNICEM 2019*, 2019.
15. A. J. George, M. Breitenbach, J. Zipprich, M. Klingler, and M. Nowottnick, "Nonconchoidal Fracture in Power Electronics Substrates due to Delamination in Baseplate Solder Joints," in *2018 7th Electronic System-Integration Technology Conference, ESTC 2018 - Proceedings*, 2018.
16. S. Zhang *et al.*, "Thermal ratchetting effect of AMB-AlN ceramic substrate: Experiments and calculations," *Ceram. Int.*, vol. 45, no. 12, 2019.
17. L. Zhu and X. Zheng, "Influence of interface energy and grain boundary on the elastic modulus of nanocrystalline materials," *Acta Mech.*, vol. 213, no. 3–4, 2010.
18. J. R. Davis, "Tensile testing (2nd ed.)," *Tensile Test.*, 2004.